*American Mineralogist, Volume 109, pages 1513–1522, 2024*

# First widespread occurrence of rare phosphate chladniite in a meteorite, winonaite Graves Nunataks (GRA) 12510: Implications for phosphide–phosphate redox buffered genesis in meteorites

**Brendan A. Anzures[1,2,*,‡], Francis M. McCubbin[3,†], Timmons M. Erickson[2], Ryan S. Jakubek[2], Marc D. Fries[3], and Loan Le[2]**

[1]Lunar and Planetary Institute, USRA, 3600 Bay Area Boulevard, Houston, Texas 77058, U.S.A.
[2]Jacobs/NASA Johnson Space Center, Astromaterials Research and Exploration Science (ARES), 2101 East NASA Parkway, Houston, Texas 77508, U.S.A.
[3]NASA Johnson Space Center, Mailcode XI, 2101 NASA Parkway, Houston, Texas 77058, U.S.A.

## Abstract

The first widespread occurrence of rare Na-, Ca-, and Mg,Mn,Fe-bearing phosphate chladniite was observed in meteorite Graves Nunataks (GRA) 12510, which is a primitive achondrite that sits within the winonaite class. Numerous 1–500 µm chladniite grains were found, often on the margins between silicate clasts and the kamacite portions of the large metal veins that permeated through the sample. The largest chladniite grains are associated with merrillite, kamacite, taenite, troilite, albite, forsterite, diopside, and enstatite, with a few tiny chladniite grains and an apatite grain enclosed within merrillite. GRA 12510s average chladniite composition is $Na_{2.7}Ca_{1.25}(Mg_{10.02}Mn_{0.69}Fe_{0.20})_{\Sigma 10.91}(PO_4)_9$. Electron backscattered diffraction (EBSD) patterns indicate varying degrees of nucleation and growth of chladniite grains. Additionally, the first pure Raman spectrum of chladniite is described here, revealing primary $\nu_1$ bands at 954, 974, and especially 984 $cm^{-1}$. The co-occurrence and close association of merrillite, apatite, chladniite, and P-bearing metallic phases within GRA 12510 suggests that the $f_{O_2}$ of IW-2 to IW-4 is an intrinsic property of the precursor chondritic material, and the phosphate-phosphide reaction may have buffered the final winonaite and IAB iron meteorite phase assemblages. Altogether, chladniite appears to form alongside other phosphates, with their chemistries reflecting the diverse environment of their formation. Meteoritic chladniite likely formed through subsolidus oxidation of schreibersite, scavenging Na from albite, Ca from diopside, Mg from enstatite/forsterite, Fe from kamacite/taenite, and Mn from alabandite/chromite when available. A $P^0$-$P^{5+}$ redox-buffered environment also has implications for thermometry and fast cooling rates, although more experiments are needed to extrapolate powder reaction rates to those of larger crystals. Furthermore, phosphide-phosphate buffered experiments may aid in investigating equilibrium chemistry at $f_{O_2}$ values between IW-2 and IW-4, which have been challenging to explore experimentally due to the limited availability of solid metal-metal oxide buffers between IW (Fe-FeO) and IW-5 (Cr-$Cr_2O_3$) at temperatures and pressures relevant to planetary interiors. Future investigations of phosphide-phosphate redox-buffered genesis at $f_{O_2}$ values between IW-2 and IW-4 have important implications for primitive meteorite constituents (e.g., CAI values), partially differentiated planetesimals and planets, including Mercury and core formation on Earth.

**Keywords:** Phosphate, phosphide, winonaite, IAB iron

## Introduction

The winonaites are a small group of primitive achondrites that provide insights into the early differentiation and partial melting of chondritic planetesimals in the early Solar System (Benedix et al. 1998, 2005; Bild 1977; Hunt et al. 2017, 2018; Zeng et al. 2019). Winonaites have not been studied in much detail since the discovery of their namesake Winona in 1928, although their number has more than doubled since 2020 from 33 to 82 through 2023 (Gattacceca et al. 2023). Winonaites are distinguished from other primitive achondrite groups based on their mineralogy and composition, reflecting reducing conditions intermediate between ordinary and enstatite chondrites (Benedix et al. 1998; Bild 1977). Winonaites are also distinguished by their oxygen isotopic systematics that bear similarities to silicate inclusions in rare group IAB complex iron meteorites, implying they formed from the same parent body (Benedix et al. 1998; Bild 1977). Winonaites are highly heterogeneous in grain size, petrologic texture, and modal mineralogy, reflecting a complex and varied geologic history (Benedix et al. 1998; Floss et al. 2007; Hunt et al. 2017; Li et al. 2011). Previous studies have revealed that winonaites experienced extensive thermal metamorphism, limited Fe-Ni-FeS partial melting, possible silicate partial melting, and catastrophic impact, breakup, and reassembly (Benedix et al. 1998, 2005; Bild 1977; Floss et al. 2007; Hunt et al. 2017, 2018; Zeng et al. 2019; Anzures et al. 2022). Studies of winonaites and IAB iron meteorites have revealed several new minerals, including rare Na- and Mg-bearing phosphates chladniite (McCoy et al.

* Corresponding author E-mail: brendan.a.anzures@nasa.gov. Orcid 0000-0002-5549-1631
† Orcid 0000-0002-2101-4431


0003-004X/24/0009–1513$05.00/DOI: https://doi.org/10.2138/am-2023-9195

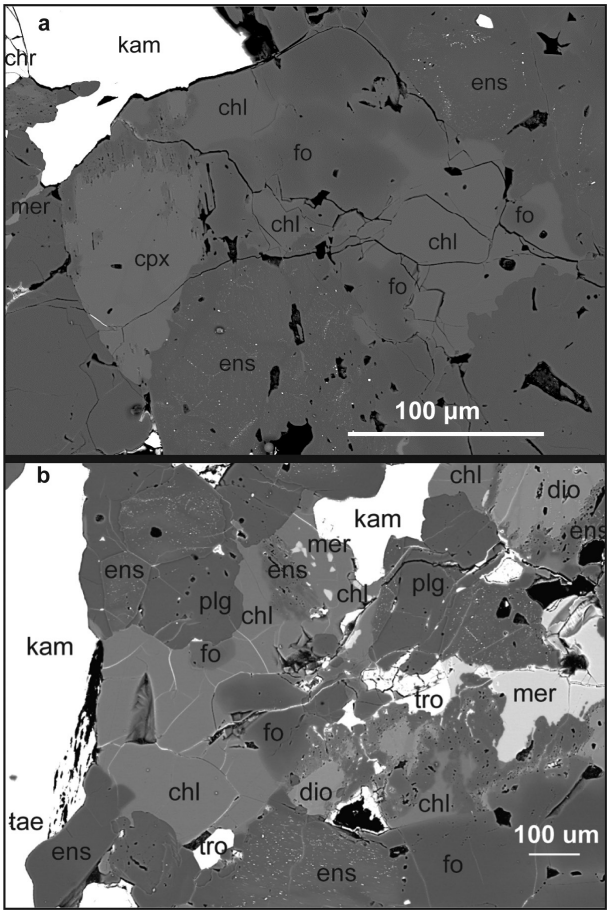


**Figure 1.** BSE image of two areas [(**a**) area A and (**b**) area B] of chladniite with associated minerals merrillite, kamacite, taenite, troilite, albite, forsterite, diopside, and enstatite.

1994), moraskoite (Karwowski et al. 2015), and czochralskiite (Karwowski et al. 2016). Here, we describe the first widespread occurrence in a meteorite of the rare Mg-rich member of the fillowite-group chladniite [$Na_3CaMg_{11}(PO_4)_9$] (Hatert et al. 2021) and its first identification in a winonaite meteorite, Graves Nunataks (GRA) 12510 (Fig. 1).

Phosphate minerals make up a minor to trace fraction of the modal mineralogy of most meteorite groups, and the most common phosphates in meteorites are apatite and merrillite (Jones et al. 2014, 2016; McCubbin et al. 2021, 2023; McCubbin and Jones 2015; Patiño Douce and Roden 2006; Ward et al. 2017). Although they are minor phases, phosphates can provide invaluable insights into the petrogenesis of samples as they are often the primary carrier of rare earth elements (REE) (Pan and Fleet 2002; Piccoli and Candela 2002). Furthermore, some phosphates can host magmatic volatiles in their structure (i.e., F, Cl, and OH) and can provide insights into the volatile history of a sample, including the isotopic compositions of H and Cl (Barnes et al. 2019, 2020; Boyce et al. 2014; McCubbin and Ustunisik 2018; Sarafian et al. 2017; Tartèse et al. 2019; Webster and Piccoli 2015). For reduced systems, like the winonaites, phosphates can also provide important constraints on oxygen fugacity as the phosphate-phosphide transition occurs at about 4 log units below the iron-wüstite (IW) buffer (IW-4) at ~700 °C and at about IW-3 at ~1300 °C (Pasek 2015). Very little is known about the phosphate mineral chladniite because it is rare in natural samples. Here we investigate the widespread occurrence of the fillowite-group mineral chladniite in winonaite GRA 12510 and its relation to the petrogenesis of GRA 12510.

## Sample material

The polished thin section studied here, GRA 12510,5, was provided by the Astromaterials Acquisition and Curation Office at NASA's Johnson Space Center and was progressively polished down before a final finish with 50 nm colloidal silica dispersion. The thin section had a 20 nm carbon coat for electron probe microanalysis (EPMA) and scanning electron microscopy (SEM) elemental mapping, which was subsequently removed and recoated with a 5 nm carbon coat for electron backscatter diffraction (EBSD). The carbon coat was then polished off for Raman spectroscopy.

## Analytical methods

### Electron probe microanalysis (EPMA)

Phase identification and quantitative major and minor element chemistry measurements were completed using electron probe microanalysis (EPMA) using the JEOL 8530 field emission (FE) electron microprobe at NASA Johnson Space Center (JSC) using a ZAF correction. Silicate minerals were analyzed using a 15 kV accelerating voltage, a 10 nA beam current, and a 5 µm spot size via wavelength-dispersive X-ray spectroscopy (WDS). Metals and sulfides were analyzed using a 15 kV accelerating voltage, 20 nA beam current, and a 1–5 µm spot size. Natural and synthetic standards were used, including canyon diablo troilite for S. Phosphates were analyzed using 15 kV accelerating voltage, 20 nA beam current, and 10 µm spot size. The analysis of phosphates, particularly apatite, followed procedures established and described in McCubbin et al. (2021). Natural and synthetic minerals were used as standards, including $SrF_2$, albite, quartz, stikin anorthite, springwater olivine, Wilberforce apatite, ilmenite, and rhodonite [crystal setup LDE1: F, TAP (Na, Si, Al, Mg), PET (P, S), PETL (Cl, Ca, Ti), and LIFH (Fe, Mn)]. Individual EPMA analyses are included in the Online Materials[1] files.

### Scanning electron microscopy (SEM)

Modal mineralogy was calculated using elemental maps produced with the JEOL 7600 scanning electron microscope (SEM) at NASA JSC. Elemental maps were collected using an accelerating voltage of 15 kV, 20 nA beam current, and 8 mm working distance at a resolution of <0.5 µm/pixel. Mineral phases were identified by the distribution of 16 elements (Na, Mg, Al, Si, P, S, K, Ca, Ti, Cr, Mn, Fe, Ni, Zn, C, O) along with energy-dispersive X-ray spectroscopy (EDS) spot analyses. Modal mineral abundances were determined by converting the elemental maps to mineralogical maps in XMapTools (Lanari et al. 2014, 2019) (Table 1; Fig. 2).

### Electron backscatter diffraction (EBSD)

Quantitative phase indexing and microstructural maps of chladniite-bearing regions were collected using the JEOL 7900F FE-SEM at NASA JSC. Electron backscatter diffraction patterns (EBSPs) were collected using an Oxford Instruments Symmetry crystal metal oxide scintillator detector and an Oxford instrument Aztec 4.1 software package. Acquisition parameters included a 20 kV accelerating voltage, 10 nA beam current, ~20 mm working distance, and a 70° tilt relative to the beam incidence. Phosphate EBSPs were indexed using a fillowite match unit after the crystal structure of Araki and Moore (1981). In addition, a merrillite match unit based on the structural data of Xie et al. (2015) was included in all maps to identify additional phosphates and ensure accurate structural indexing of the grains. Maps were collected with a step size ranging from 0.5–0.2 µm.

Post-processing of the EBSD data used Oxford Instruments Aztec Crystal 2.2 program. All EBSD data were given a wild-spike noise reduction and a seven nearest neighbor zero-solution correction. An additional correction was applied to remove systematic misindexing of the fillowite data with disorientation relation of 180° <11–20> caused by mirror symmetry normal to the axis. Forescatter electron,

**Table 1.** Modal abundance of minerals in GRA 12510 (by area %)

| | |
|---|---|
| Enstatite | 27.89 |
| Diopside | 4.10 |
| Albite | 11.49 |
| Forsterite | 20.04 |
| Chromite | 0.83 |
| Kamacite | 25.92 |
| Taenite | 4.54 |
| Schreibersite | 1.09 |
| Troilite | 2.88 |
| Alabandite | Trace |
| Chladniite | 0.78 |
| Merrillite | 0.45 |
| Apatite | Trace |

EBSD phase, and inverse pole figure (IPF) maps can be found in Figure 3. Fillowite pole plots are equal area, lower hemisphere projections.

### Raman spectroscopy and Raman spectroscopic imaging

Chladniite and its associated minerals were measured using a WITec alph300R Raman microscope (XMB3000-3003) at NASA JSC. Both single spectra and a Raman image were collected. Incident 532 or 488 nm excitation was generated using a WITec diode laser (XSL3100-1154), producing ~170 µW or ~100 µW of incident power at the sample surface, respectively. For single spectral collections, the incident laser was focused on the sample surface using either a 100× magnification Zeiss EC Epiplan-Neofluar objective producing a 0.9 µm beam spot on the sample surface or a 50× magnification Zeiss EC Epiplan objective producing a 1.2 µm spot size on the sample surface. The Raman scattered light was dispersed using a WITec UHTS600 (XMC3200-0600) spectrometer with a 300 g/mm grating, and the spectrum was detected using a back-illuminated, thermoelectrically cooled (–60 °C) CCD (XMC3022-1001). Single spectra were collected by averaging ~5–10 accumulations, each with a 10 s integration time. The Raman image of 100 × 100 spectra was collected over a 300 × 300 µm area of the sample for a Raman image resolution of 3 µm/pixel and a total of 10 000 individual spectra. The 50× magnification objective was used to collect the Raman image. The accumulation time for each individual Raman spectrum in the image was 5 s for an image accumulation time of 14 h and 8 min. Principal component analysis (PCA) of the image was performed using WITec Project FIVE software to identify and map the main component minerals chladniite, merrillite, enstatite, diopside, olivine, and feldspar as shown in Figure 4a. Representative Raman spectra of chladniite and merrillite, as well as fillowite from the literature, are shown in Figure 4b.

## Results

### Occurrence

GRA 12510 is a coarse-grained winonaite with abundant metal veins and pools separating silicate clasts that are either dominated by orthopyroxene or orthopyroxene+olivine. Modal mineralogy is 65.43% silicate (28.27% orthopyroxene, 21.63% olivine, 4.54% clinopyroxene, and 10.87% plagioclase), 30.01% metal (26.08% kamacite, 3.50% taenite, and 0.43% schreibersite), with minor troilite (2.73%), chromite (0.50%), merrillite (1.13%), chladniite (0.32%), and trace apatite (Table 1; Fig. 2). Both silicate clast lithologies have similar silicate:metal area% ratios (84.33:8.15 and 85.11:10.77 for the orthopyroxene-rich and orthopyroxene + olivine-rich clasts). However, the orthopyroxene-rich clasts have more

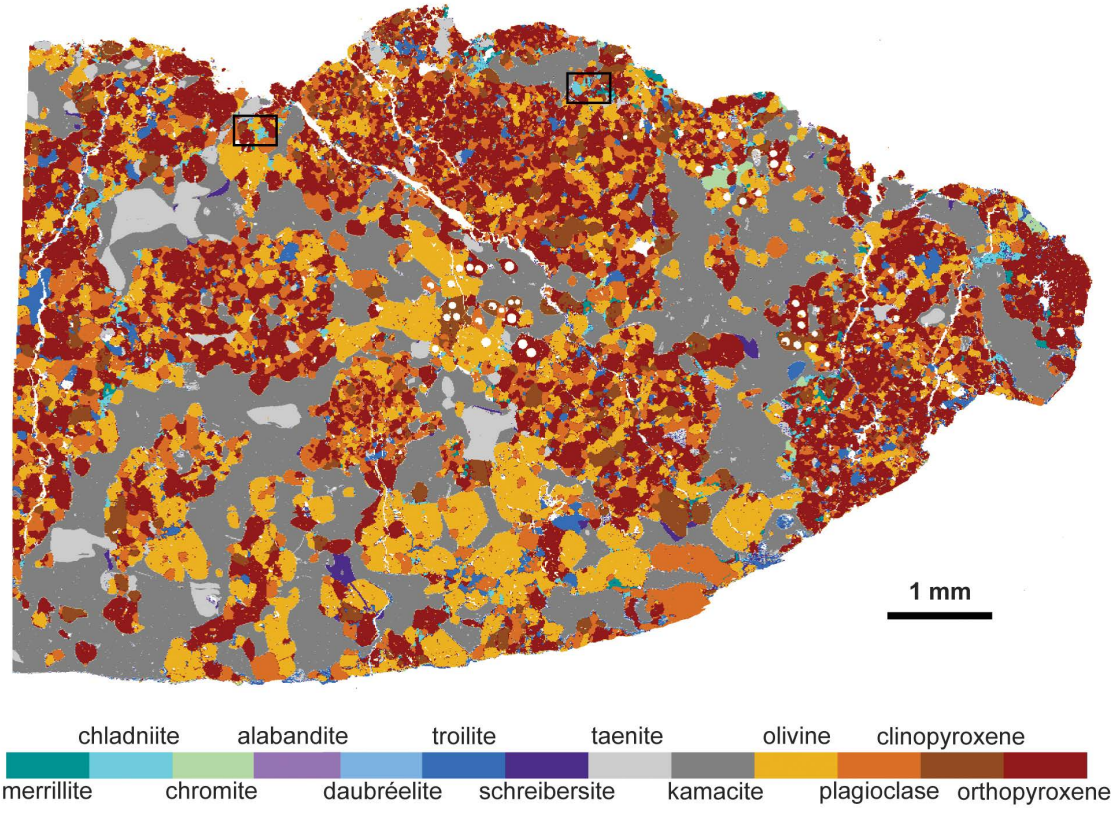


**Figure 2.** Mineralogical map of GRA 12510. Chladniite grains from 1–200 µm are scattered throughout the section often on margins between silicate clasts and metal. The areas immediately surrounding chladniite are mostly Mn free, but several Mn-rich chromite grains (7.89 wt% MnO) and one tiny alabandite grain (MnS) are found elsewhere in the section. Schreibersite is also anti-correlated with chladniite. Black box insets correspond to areas A and B in Figure 1. White circles are 75–150 µm LA-ICP-MS pits from previous trace element analyses.

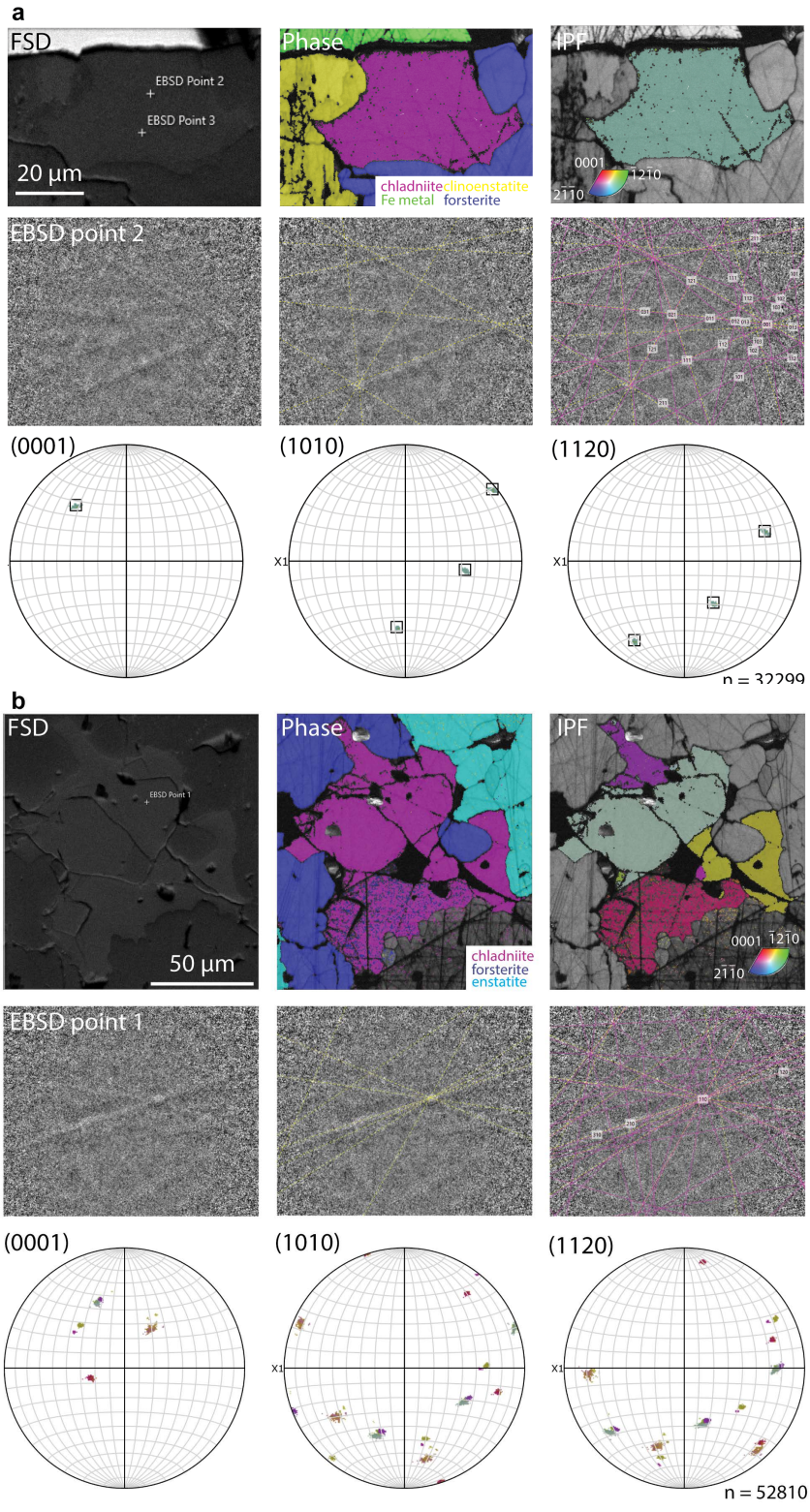


**FIGURE 3.** EBSD data of three occurrences of chladniite [(**a**) area A, (**b**) area A, (**c**) area B] and its associated mineral assemblages with forward scattered electron diode (FSD), phase overlay, and inverse pole (IPF) images along with the Kikuchi patterns, Kikuchi bands, and Kikuchi solutions as well as pole figures {0001}, {10$\bar{1}$0}, and {11$\bar{2}$0}. *(Figure continues on next page.)*

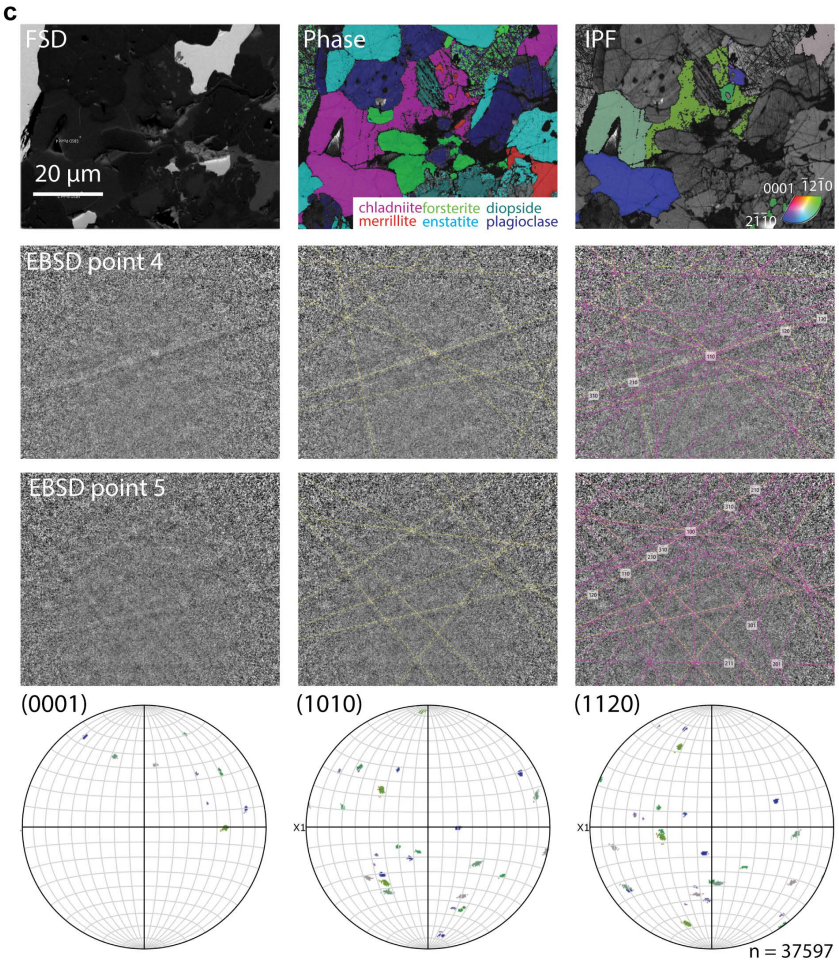


**FIGURE 3.—*CONTINUED.***

orthopyroxene (45.05 vs. 31.68%), less clinopyroxene (5.36 vs. 11.09%), similar abundances of plagioclase (12.85 vs. 11.64%), and less olivine (21.07 vs. 30.70%). A single 5 µm diameter grain of alabandite (MnS) was also found in an orthopyroxene-rich silicate clast in contact with troilite and schreibersite. A single F-rich, Cl-bearing apatite grain was found as an inclusion in merrillite. Notably, the orthopyroxene-rich clast has substantially more phosphate (0.67% chladniite and 1.66% merrillite vs. 0.31% chladniite and 1.23% merrillite) and less phosphide (0.09% vs. 0.81% schreibersite).

Numerous 1–500 µm chladniite grains were found, often on the margins between silicate clasts and the kamacite portions of the large metal veins. The largest chladniite grains are associated with merrillite, kamacite, taenite, troilite, albite, forsterite, diopside, and enstatite (Fig. 2). Rarely, chladniite encloses <3 µm merrillite grains as seen in Figure 2b. Additionally, even though chladniite in this meteorite contains Mn, the areas immediately surrounding chladniite are mostly Mn free. However, several Mn-rich chromite grains (7.89 wt% MnO) and one tiny alabandite grain (MnS) are found elsewhere in the section.

### Composition of chladniite

The average composition of 37 analyses of 7 grains of chladniite in GRA 12510 is shown in Table 2. These chladniite grains include those near metal, merrillite, and silicates, as well as inclusions in merrillite and albite. Based on these analyses, the calculated mineral formula for chladniite in GRA 12510 is $Na_{2.7}Ca_{1.25}(Mg_{10.02}Mn_{0.69}Fe_{0.20})_{\Sigma 10.91}(PO_4)_9$ after the paper of Hatert et al. (2021), stoichiometry $Na_3CaMg_{11}(PO_4)_9$.

### EBSD

EBSD analyses of GRA 12510 revealed that the chladniite structure agreed well with fillowite (Araki and Moore 1981), thus falling within the fillowite-type phosphate group. Chladniite areas were found using forescatter electron images (Fig. 3). Diffraction patterns were collected from one large chladniite grain in area A, as well as chladniite areas with multiple grain boundaries in area A and B (areas A and B matching those identified in BSE images in Fig. 1). The mean angular deviation values of the electron backscatter patterns for the maps ranged between 0.87 to 0.63 for fillowite-structure materials, corroborating the chladniite-type phosphate.

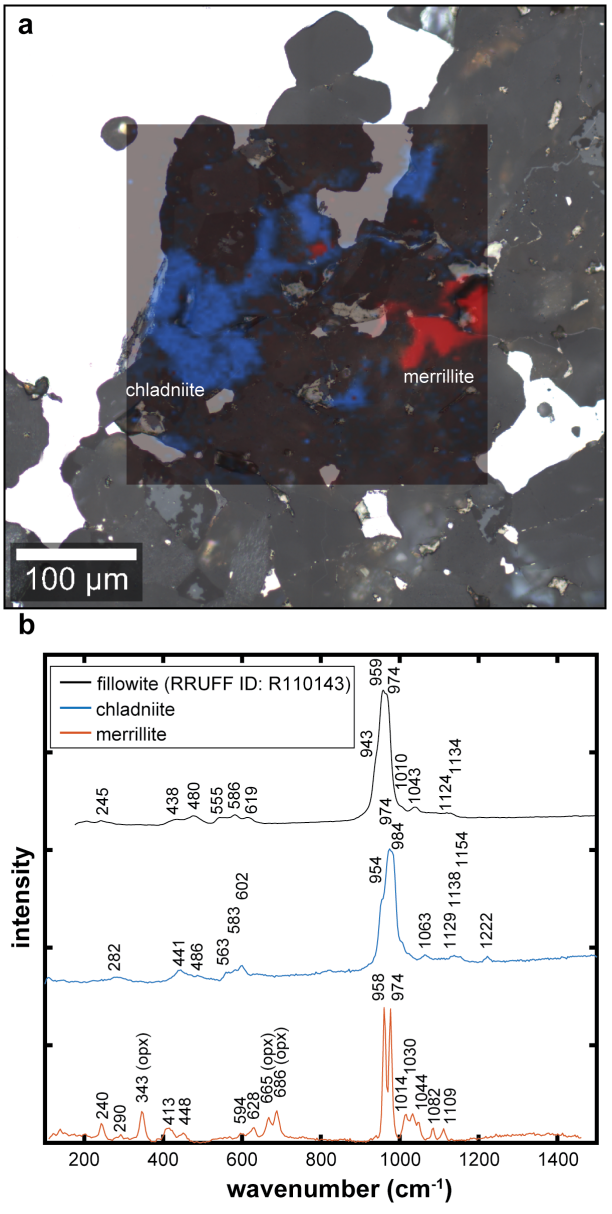


**FIGURE 4.** (**a**) Raman image overlaying an optical microscope image exhibiting the distribution of chladniite and merrillite in area B of GRA 12510. (**b**) Raman spectra of chladniite compared with merrillite and fillowite (RRUFF ID: R110143).

Crystallographic orientations displayed as IPP maps and pole plots showed a single 40 × 60 µm chladniite grain in area A (Fig. 3a). Other chemically coherent chladniite areas including a 100 × 100 µm area (Fig. 3b) and an ~500 µm diameter area (Fig. 3c) were actually revealed through EBSD to be monomineralic granular aggregates with grain sizes down to 3 µm. The pole plots do not show a systematic pattern consistent with preferred growth orientation, but rather with multiple random orientations, indicating nucleation and coalescence of grains (Prior et al. 1999).

**TABLE 2.** Average major element compositions (wt%) of phosphates (chladniite, merrillite, and apatite), silicates and oxides (forsterite, enstatite, diopside, albite, and chromite), metals (kamacite, taenite, schreibersite), and sulfides (troilite, alabandite) in GRA 12510 from EPMA

| | Phosphates | | |
|---|---|---|---|
| wt% | Chladniite | Merrillite | Apatite |
| $SiO_2$ | 0.25 (16) | b.d.l. | b.d.l. |
| $TiO_2$ | 0.03 (00) | b.d.l. | b.d.l. |
| FeO | 1.14 (10) | 0.32 (30) | 0.75 |
| MnO | 3.92 (12) | 0.19 (3) | 0.16 |
| MgO | 32.58 (26) | 3.78 (6) | 0.13 |
| CaO | 5.62 (3) | 46.23 (21) | 53.57 |
| $Na_2O$ | 6.75 (5) | 2.75 (3) | 0.08 |
| $P_2O_5$ | 51.22 (25) | 47.14 (39) | 42.02 |
| F[a] | | | 2.38 |
| Cl | | | 2.51 |
| S | | | 0.01 |
| –O=F+Cl+S | | | 1.65 |
| Total | 101.51 (31) | 100.42 (33) | 99.96 |
| *N* | **37** | **20** | **1** |

| | Silicates and oxides | | | | |
|---|---|---|---|---|---|
| wt% | Forsterite | Enstatite | Diopside | Albite | Chromite |
| $SiO_2$ | 42.06 (21) | 59.95 (9) | 54.91 (20) | 65.55 (52) | 0.02 (1) |
| $TiO_2$ | b.d.l. | 0.02 (0) | 0.68 (4) | 0.04 (1) | 0.20 (6) |
| $Al_2O_3$ | b.d.l. | 0.03 (0) | 0.81 (6) | 21.38 (17) | 0.46 (47) |
| $Cr_2O_3$ | | | | | 70.38 (52) |
| FeO | 3.11 (84) | 0.48 (2) | 1.06 (14) | 0.29 (17) | 13.77 (64) |
| MnO | 0.97 (31) | 0.24 (0) | 0.36 (3) | 0.01 (1) | 7.89 (79) |
| MgO | 55.51 (92) | 40.18 (0) | 18.73 (17) | 0.01 (1) | 6.05 (16) |
| CaO | 0.02 (1) | 0.65 (13) | 22.09 (26) | 2.38 (22) | 0.01 (1) |
| $Na_2O$ | b.d.l. | 0.01 (1) | 0.72 (5) | 9.89 (16) | |
| $V_2O_3$ | | | | | 0.40 (13) |
| ZnO | | | | | 1.30 (4) |
| Total | 101.67 | 101.55 | 99.36 | 99.56 | 100.48 |
| *N* | 4 | 2 | 6 | 12 | 13 |

| | Metals and sulfides | | | | |
|---|---|---|---|---|---|
| wt% | Kamacite | Taenite | Schreibersite | Troilite | Alabandite |
| S | b.d.l. | b.d.l. | | 36.16 (71) | 36.80 (10) |
| P | 0.04 (2) | 0.01 (1) | 15.02 (4) | 0.01 (1) | |
| Si | 0.02 (1) | 0.02 (2) | 0.01 (0) | 0.04 (1) | 0.03 (2) |
| Mg | 0.01 (1) | b.d.l. | | 0.02 (1) | 0.02 (1) |
| Ca | 0.01 (1) | 0.01 (1) | | 0.07 (5) | 0.01 (1) |
| Mn | 0.01 (1) | b.d.l. | | 0.02 (2) | 58.03 (29) |
| Ni | 6.17 (34) | 25.34 (70) | 48.28 (71) | 0.02 (2) | 0.14 (6) |
| Cr | b.d.l. | b.d.l. | | 0.06 (2) | b.d.l. |
| Mo | b.d.l. | 0.01 (1) | | b.d.l. | b.d.l. |
| Fe | 93.59 (133) | 75.63 (63) | 36.73 (60) | 62.36 (52) | 4.81 (19) |
| Co | 0.55 (2) | 0.25 (2) | 0.11 (1) | 0.08 (1) | |
| Total | 100.42 (140) | 101.29 (23) | 100.14 (40) | 98.84 (92) | 99.83 (32) |
| *N* | 29 | 5 | 20 | 7 | 5 |

*Notes*: *N* = number of analyses. b.d.l. = abundance was below detection limit. All parenthetical values represent 1-sigma standard deviation of the mean.
[a] *X*-site sum exceeded 1 structural formula unit so F was computed assuming $X_F = 1 - X_{Cl}$ using the methods outlined in McCubbin et al. (2021).

## RAMAN SPECTROSCOPY

Here, the Raman spectra of pure chladniite are described for the first time, revealing a diagnostic peak centered at 982 $cm^{-1}$, as shown in Figure 4b. A previous attempt at collecting a Raman spectrum of chladniite in a type III silicate-phosphate (PG) inclusion in the Elga IIE iron meteorite resulted in a predominantly merrillite spectrum with a chladniite shoulder at 984 $cm^{-1}$ (Litasov and Podgornykh 2017). Phosphates typically have a main peak corresponding to the $\nu_1$ symmetric stretching mode of $PO_4^{3-}$ at 950–990 $cm^{-1}$, an antisymmetric $\nu_3$ vibration at 1000–1175 $cm^{-1}$, as well as weaker bands due to the $\nu_2$ bending mode at 400–500 $cm^{-1}$, $\nu_4$ bending mode at 550–640 $cm^{-1}$, and lattice modes at wavenumbers lower than 300 $cm^{-1}$ (Litasov and Podgornykh 2017). Chladniite appears to have three strong overlapping $\nu_1$ bands at 954, 974, and

984 $cm^{-1}$, $\nu_3$ bands at 1063, 1129, 1138, and 1154 $cm^{-1}$, $\nu_2$ bands at 441 and 486 $cm^{-1}$, $\nu_4$ bands at 563, 583, and 602 $cm^{-1}$, and lattice mode bands at 282 $cm^{-1}$. Although chladniite is isostructural with fillowite, the substitution of Mg for $Mn^{2+}$ in chladniite affects the $\nu_1$ vibrational frequencies. Fillowite has three $\nu_1$ bands at 943, 959, and 974 $cm^{-1}$ (RRUFF database), whereas chladniite shows $\nu_1$ bands at 954, 974, and 984 $cm^{-1}$. Three strong overlapping $\nu_1$ bands indicate that the $PO_4$ tetrahedra inhabits three non-equivalent positions with slight structural/environmental heterogeneity rather than a more uniform location in its crystal structure.

## Discussion

### Winonaite parent body pressure-temperature-redox conditions

There are some thermodynamic constraints on the formation conditions of the winonaite parent body that can be used to elucidate the formation of chladniite. The winonaite parent body has been estimated to be a small body with a radius of ~100 km (Benedix et al. 2005) that corresponds to a maximum pressure of 0.01 GPa (Lucas et al. 2020). The winonaite parent body is also reduced, with silicates recording oxygen fugacities ($f_{O_2}$) from IW-2.3 to IW-3.2 calculated using the FeO content of olivine (quartz-iron-fayalite) and pyroxene (quartz-iron-ferrosillite) (Benedix et al. 2005). In their study, Benedix et al. (2005) note that winonaite and IAB $f_{O_2}$ estimates do not fall along any traditional metal-metal oxide buffers or the temperature and pressure-dependent graphite-carbon monoxide buffer. However, this $f_{O_2}$ range calculated from the silicates is consistent with the phosphide-phosphate oxidation transition of IW-3 to IW-4 designated by the schreibersite ($Fe_3P$)-whitlockite [$Ca_3(PO_4)_2$] buffer (Bindi et al. 2023; Pasek 2015) as shown in Figure 5. Recent experiments also suggest that at temperatures >900 °C, the phosphide-to-phosphate reaction occurs rapidly, with complete oxidation from phosphide within a week and a few percent reduction of phosphate on the same timescale (Feng and Pasek 2023). The co-occurrence and close association of merrillite, chladniite, apatite, and P-bearing metallic phases within GRA 12510 suggests that the $f_{O_2}$ of IW-2 to IW-4 is an intrinsic property of the precursor chondritic material and the phosphate-phosphide reaction may have buffered the final winonaite and IAB iron meteorite phase assemblages.

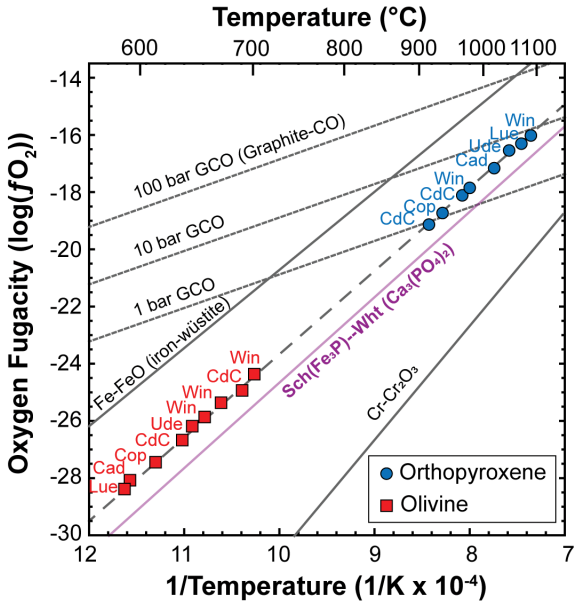


**Figure 5.** Plot of oxygen fugacity ($\log f_{O_2}$) vs. temperature [10 000/$T$(K)] for IAB irons and a winonaite along with appropriate oxygen fugacity buffers adapted from Benedix et al. (2005). Oxygen fugacity determined from orthopyroxene (blue) and olivine (red) for meteorites Cad (Caddo County), CdC (Campo del Cielo), Cop (Copiapo), Lue (Lueders), Ude (Udei Station), Win (Winona) with data falling along the dashed best fit line. Winonaite and IAB iron meteorite oxygen fugacities fall along the schreibersite ($Fe_3P$) – whitlockite [$Ca_3(PO_4)_2$] buffer purple line (Pasek 2015; Bindi et al. 2023) indicating these meteorites were likely redox buffered by the present phase assemblage of phosphide (P valence state of 0) and phosphate (P valence state of 5+). Also shown are three CO-C fugacity buffers at different pressures that fall on a different slope.

The prevailing model for winonaite-IAB parent body formation is that it underwent incomplete differentiation followed by catastrophic impact, breakup, and reassembly (Benedix et al. 2000). Most recently, the proposed layered structure of the winonaite-IAB iron meteorite parent body from the surface to the core was: (1) precursor chondritic material; (2) diverse lithologies that experienced limited metamorphism and FeNi-FeS partial melting; (3) residues of silicate partial melting; and (4) incompletely differentiated molten metal represented by IAB iron meteorites (Hunt et al. 2017; Zeng et al. 2019). Adding onto this model, winonaite and IAB iron meteorites record rapid cooling rates of 0.48–1.75 °C/year, and therefore cooled from their peak magmatic temperatures as collisional fragments during breakup prior to reassembly (Anzures et al. 2022). Finally, the winonaite parent body also experienced multiple impact events that caused liberation from the parent body before impacting and being found on Earth. Cosmic-ray exposure ages for winonaites range from 0.02 to 0.08 Ga (Benedix et al. 1998), while IAB iron meteorites range from 0.4 to 1.0 Ga (Voshage 1967).

### Origin of chladniite

The only other occurrences of chladniite have been as a single large grain in a complex silicate-bearing inclusion in IAB iron meteorite Carlton (McCoy et al. 1994), a minor phase in lodranite GRA 95209 (Floss 1999; Grew et al. 2010; McCoy et al. 2006; McCoy and Carlson 1998), as inclusions in merrillite-dominated phosphate aggregate in a IIE iron meteorite Elga (Litasov and Podgornykh 2017), in a couple of terrestrial pegmatites in Argentina (Vallcorba et al. 2017) and Brazil (Hatert et al. 2021), and as a REE-bearing Y-chladniite in a granulite from Antarctica (Grew et al. 2006). The first terrestrial identification of chladniite was found in a pegmatite from Córdoba, Argentina, as up to 200 μm diameter inclusions in beusite, the Mn analog of the graftonite phosphate structural group (Vallcorba et al. 2017). Based on chemical and textural evidence, the association of beusite and chladniite was interpreted as a replacement product of garnet during the magmatic stage (Vallcorba et al. 2017) caused by destabilization of garnet due to phosphorous buildup (Colombo et al. 2012). Chladniite has also been found in another pegmatite in Sapucaia, Brazil (Hatert et al. 2021). Y-chladniite

was also found in a granulite in Larsemann Hills, Antarctica as up to 250–1000 µm inclusions in fluorapatite associated with wagnerite, xenotime-(Y), monazite-(Ce), P-bearing K-feldspar, biotite, sillimanite, quartz, and pyrite. Y-chladniite was inferred to have formed at 800–860 °C and 0.6–0.7 GPa by reaction of biotite with an anatectic melt with phosphorous buildup by interaction with fluorapatite (Grew et al. 2006). However, terrestrial chladniite likely has a different mode of formation than meteoritic chladniite because of the much higher pressures and more oxidizing environments on Earth, as well as the inferred differences in geological processes that occur on small asteroids vs. the Earth's crust.

For meteoritic chladniite formation, two hypotheses for its formation are either as a: (1) replacement product of a phosphate [either graftonite (Floss 1999) or panethite (Litasov and Podgornykh 2017)], which originated by reaction of olivine and orthopyroxene with metallic iron containing P or (2) crystallization from the reaction of plagioclase and pyroxene with metallic iron or schreibersite (Floss 1999). In lodranite GRA 95209, chladniite is also associated with a graftonite structural group phosphate in the iron analog graftonite as <50 µm thick veins intersecting silicate phases adjacent to remnant metal or troilite (Floss 1999). However, in IAB iron meteorite Carlton, the single chladniite grain (175 × 975 µm) is not associated with a graftonite group phosphate, but rather with chlorapatite. In IIE iron meteorite Elga, chladniite was found in only one site as <10 µm inclusions in merrillite surrounded by schreibersite rims and enclosed within kamacite-taenite metal (Litasov and Podgornykh 2017). In Elga, chladniite was suggested to be poorly crystalline due to its Raman spectra always being contaminated by merrillite peaks (Litasov and Podgornykh 2017).

Chladniite in winonaite GRA 12510 is much more abundant and found in larger grain sizes here compared with other meteorites. Numerous 1–500 µm chladniite grains were found, often on the margins between silicate clasts and the kamacite portions of the large metal veins. The largest chladniite grains are associated with merrillite, kamacite, taenite, troilite, albite, forsterite, diopside, and enstatite (Fig. 2). Additionally, unlike Elga where a few tiny poorly crystallized chladniite grains are included in merrillite (Litasov and Podgornykh 2017), sometimes chladniite in GRA 12510 encloses <3 µm merrillite grains as seen in Figure 2b.

Chladniite compositions differ widely, which suggests that the composition is controlled by the geologic environment of formation rather than by crystal-chemical constraints (Vallcorba et al. 2017). Terrestrial pegmatitic chladniite has high Mn and Fe (13.96–14.42 wt% MnO and 15.98–17.37 wt% FeO) reflective of its pegmatitic environment (Hatert et al. 2021; Vallcorba et al. 2017) and association with Mn-phosphate beusite in Argentina (Vallcorba et al. 2017). Terrestrial granulite chladniite has similar Fe content (15.88 wt% FeO) but virtually no Mn (0.26 wt% MnO) due to its almost Mn-free environment (Grew et al. 2006). The chladniite of lodranite GRA 95209 is also rich in Fe with a little less Mn [8.61 wt% MnO and 14.4 wt% FeO (Floss 1999)] reflective of its association with Fe-phosphate graftonite. Chladniite in silicate clasts of iron meteorites has very low Mn and Fe, including IAB iron Carlton (0.30 MnO and 2.23 wt% FeO, respectively) (McCoy et al. 1994) and IIE Elga (1.37 MnO and 5.11 wt% FeO) (Litasov and Podgornykh 2017). GRA 12510s chladniite also has relatively low overall Mn and Fe (3.92 wt% MnO and 1.14 wt% FeO, respectively). However, GRA 12510s chladniite is 10 times higher in Mn than in Carlton, which could have been scavenged from MnS or Mn-rich chromite that are spatially anti-correlated with abundant chladniite in the sample. Interestingly, this composition plots slightly within the proposed miscibility gap in a $Fe^{2+}$-Mn-Mg ternary for fillowite-type phosphates (Fransolet et al. 1998; Hatert et al. 2021), as shown in Figure 6. This possible miscibility gap has been hypothesized because of the larger difference in ionic radii between Mg and Mn compared with their similarities to $Fe^{2+}$, although this could also be due to small sample bias with only seven total occurrences of chladniite.

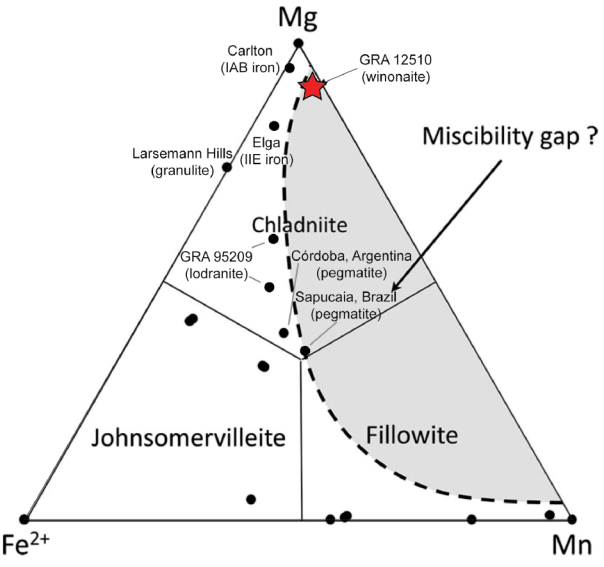


**FIGURE 6.** Ternary $Fe^{2+}$-Mn-Mg diagram of natural fillowite-type phosphates. The most Mn-rich analysis of chladniite in GRA 12510 falls slightly within the proposed miscibility gap of Hatert et al. (2021).

Altogether, chladniite appears to form alongside other phosphates, with their chemistries reflecting the diverse environment of their formation. Meteoritic chladniite likely formed through subsolidus oxidation of schreibersite $(Fe,Ni)_3P$ scavenging Na from albite, Ca from diopside, Mg from enstatite/forsterite, Fe from kamacite/taenite, and Mn from alabandite/chromite when available. Near Mg-end-member enstatite and forsterite (Mg# >90) are generally the most abundant mineral aside from metal in winonaites, IAB irons, and lodranites, consistent with the Mg-, rather than Fe- or Mn-, end-member of the fillowite group being present in GRA 12510. Whereas Carlton likely formed in a Cl-rich environment with chlorapatite present (McCoy et al. 1994), and GRA 95209 formed in a Cl-poor and Fe-rich environment (Floss 1999). Although Elga has both chladniite, merrillite, and schreibersite like GRA 12510, its silicates appear to be more oxidized with an average orthopyroxene composition of $En_{76}Fs_{21.5}Wo_{2.5}$. Elga's lower Mn in chladniite compared with GRA 12510 is also reflected in its Mn-poor chromite (2.15 vs. 7.89 wt% MnO) and the presence of only troilite rather than troilite and alabandite, respectively.

## IMPLICATIONS

This schreibersite-chladniite reaction appears to have buffered the redox state of GRA 12510 with the recorded $f_{O_2}$ using FeO content of olivine (quartz-iron-fayalite) and pyroxene (quartz-iron-ferrosillite) in winonaites/IAB iron meteorites (Benedix et al. 2005) corresponding to the $f_{O_2}$-$T$ curve of the phosphide-phosphate buffer (Bindi et al. 2023; Pasek 2015). The primary texture of the schreibersite and the secondary texture of the chladniite suggest that GRA 12510 was initially reduced. Furthermore, within a single section of GRA 12510 studied here, chladniite makes up a higher fraction of the modal mineralogy than schreibersite, suggesting that this reaction was proceeding toward oxidation at the time of closure. Schreibersite-chladniite and, more broadly, schreibersite-phosphate assemblages in other meteorites, including IAB iron Carlton, IIE iron Elga, lodranite GRA 95209, indicate they formed in a $P^0$-$P^{5+}$ redox-buffered environment with an oxygen fugacity of ~IW-3 to IW-4 dependent on temperature.

A $P^0$-$P^{5+}$ redox-buffered environment also has implications for thermometry and cooling rates. Recent experiments found that at >900 °C (close to the closure temperatures of common silicates such as clinopyroxene, orthopyroxene, and plagioclase), the phosphide to phosphate reaction occurs rapidly with a few % oxidation from phosphide within days and complete oxidation within a week, along with a few percent reduction of phosphate on the same timescale (Feng and Pasek 2023). These experiments using powdered reagents suggest that a phosphide-phosphate phase assemblage would only be preserved if cooling rates were quite fast in the presence of an available oxidant, much faster than the fastest cooling rates estimated for high-temperature meteorite equilibration at 10–100 °C/year for ordinary chondrites (Lucas et al. 2020). However, those estimated cooling rates may not be a good analogy for the larger crystals that are present in the interiors of asteroid parent bodies. Given that closure temperatures are proportional to grain size squared (Dodson 1973), grains twice as large will cool four times more slowly for a given closure temperature. Therefore, to truly constrain cooling rates of phosphide-phosphate phase assemblages, more experiments are needed to constrain solid-state phosphide oxidation and phosphate reduction timescales for realistic grain sizes in meteorites.

Furthermore, phosphide-phosphate buffered experiments may aid in investigating equilibrium chemistry at $f_{O_2}$ values between IW-2 and IW-4, which have been challenging to explore experimentally due to the limited availability of solid metal-metal oxide buffers between IW (Fe-FeO) and IW-5 (Cr-$Cr_2O_3$) at temperatures and pressures relevant to planetary interiors. This $f_{O_2}$ range is of particular interest for understanding changes in S speciation that have been highlighted by Anzures et al. (2020), where the dominant S species in silicate melt changes from FeS at $f_{O_2}$ >IW-2 to MgS at $f_{O_2}$ <IW-4, with a few experiments suggesting that CaS/$Na_2S$ are the major species at IW-2 to IW-4. There is a growing recognition that such low-$f_{O_2}$ conditions (IW-2 to IW-4) were widespread and had a significant control on the formation of planetary bodies in the early solar system, including primitive meteorite constituents CAI values, type I CR chondrites, and CM refractory inclusions, partially differentiated planetesimals that sourced the winonaite-IAB iron, lodranite-acapulcoite, ureilite, IIE iron, and IIICD iron meteorites (Righter et al. 2016), and finally planets on the oxidized range for Mercury (IW-3 to IW-7) (McCubbin et al. 2012; Nittler et al. 2023; Zolotov et al. 2013) and reduced estimate for Earth's core formation (IW-2 to IW-3.5) (Badro et al. 2015; Dauphas 2017; Fischer et al. 2017).

## ACKNOWLEDGMENTS AND FUNDING

We are grateful to the Meteorite Working Group, now the Antarctic Meteorite Review Panel of the Astromaterials Allocation Review Board, for carefully evaluating our sample requests, and we thank the curatorial staff at NASA Johnson Space Center for the allocation of the Antarctic meteorites used in this study. The U.S. Antarctic meteorite samples are recovered by the Antarctic Search for Meteorites (ANSMET) program, which has been funded by NSF and NASA and characterized and curated by the Department of Mineral Sciences of the Smithsonian Institution and Astromaterials Acquisition and Curation Office at NASA Johnson Space Center, respectively. We are grateful to associate editor Oliver Tschauner and editor Hongwu Xu for the editorial handling of this manuscript and to the reviewers who provided constructive and helpful comments. Support for this research was provided by NASA's Planetary Science Division Research Program, through ISFM work package's Planetary Process Simulation and Cosmochemistry/Geochemistry at NASA Johnson Space Center. B.A.A., T.M.E., R.S.J., and L.L. acknowledge support from the JETSII contract at NASA Johnson Space Center.

## REFERENCES CITED

Anzures, B.A., Parman, S.W., Milliken, R.E., Namur, O., Cartier, C., and Wang, S. (2020) Effect of sulfur speciation on chemical and physical properties of very reduced mercurian melts. Geochimica et Cosmochimica Acta, 286, 1–18, https://doi.org/10.1016/j.gca.2020.07.024.

Anzures, B.A., Dygert, N., and Lucas, M. (2022) Thermochemical evolution of the winonaite and IAB iron meteorite parent body. Proceedings of the 53rd Lunar and Planetary Science Conference, p. 2696. Lunar and Planetary Institute, Woodlands, Texas.

Araki, T. and Moore, P.B. (1981) Fillowite, $Na_2Ca(Mn,Fe)_7^{2+}(PO_4)_6$: Its crystal structure. American Mineralogist, 66, 827–842.

Badro, J., Brodholt, J.P., Piet, H., Siebert, J., and Ryerson, F.J. (2015) Core formation and core composition from coupled geochemical and geophysical constraints. Proceedings of the National Academy of Sciences of the United States of America, 112, 12310–12314, https://doi.org/10.1073/pnas.1505672112.

Barnes, J.J., Franchi, I.A., McCubbin, F.M., and Anand, M. (2019) Multiple reservoirs of volatiles in the Moon revealed by the isotopic composition of chlorine in lunar basalts. Geochimica et Cosmochimica Acta, 266, 144–162, https://doi.org/10.1016/j.gca.2018.12.032.

Barnes, J.J., McCubbin, F.M., Santos, A.R., Day, J.M.D., Boyce, J.W., Schwenzer, S.P., Ott, U., Franchi, I.A., Messenger, S., Anand, M., and others. (2020) Multiple early-formed water reservoirs in the interior of Mars. Nature Geoscience, 13, 260–264, https://doi.org/10.1038/s41561-020-0552-y.

Benedix, G.K., McCoy, T.J., Keil, K., Bogard, D.D., and Garrison, D.H. (1998) A petrologic and isotopic study of winonaites: Evidence for early partial melting, brecciation, and metamorphism. Geochimica et Cosmochimica Acta, 62, 2535–2553, https://doi.org/10.1016/S0016-7037(98)00166-5.

Benedix, G.K., McCoy, T.J., Keil, K., and Love, S.G. (2000) A petrologic study of the IAB iron meteorites: Constraints on the formation of the IAB-Winonaite parent body. Meteoritics & Planetary Science, 35, 1127–1141, https://doi.org/10.1111/j.1945-5100.2000.tb01502.x.

Benedix, G.K., Lauretta, D.S., and McCoy, T.J. (2005) Thermodynamic constraints on the formation conditions of winonaites and silicate-bearing IAB irons. Geochimica et Cosmochimica Acta, 69, 5123–5131, https://doi.org/10.1016/j.gca.2005.03.048.

Bild, R.W. (1977) Silicate inclusions in group IAB irons and a relation to the anomalous stones Winona and Mt Morris (Wis). Geochimica et Cosmochimica Acta, 41, 1439–1456, https://doi.org/10.1016/0016-7037(77)90250-2.

Bindi, L., Feng, T., and Pasek, M.A. (2023) Routes to reduction of phosphate by high-energy events. Communications Earth & Environment, 4, 70, https://doi.org/10.1038/s43247-023-00736-2.

Boyce, J.W., Tomlinson, S.M., McCubbin, F.M., Greenwood, J.P., and Treiman, A.H. (2014) The lunar apatite paradox. Science, 344, 400–402, https://doi.org/10.1126/science.1250398.

Colombo, F., Sfragulla, J., and Del Tánago, J.G. (2012) The garnet - phosphate buffer in peraluminous granitic magmas: A case study from pegmatites in the Pocho district, Córdoba, Argentina. Canadian Mineralogist, 50, 1555–1571, https://doi.org/10.3749/canmin.50.6.1555.

Dauphas, N. (2017) The isotopic nature of the Earth's accreting material through time. Nature, 541, 521–524, https://doi.org/10.1038/nature20830.

Dodson, M.H. (1973) Closure temperature in cooling geochronological and petrological systems. Contributions to Mineralogy and Petrology, 40, 259–274, https://doi.org/10.1007/BF00373790.

Feng, T. and Pasek, M.A. (2023) Thermal phosphide mineral oxidation chemistry. Proceedings of the 54th Lunar and Planetary Science Conference, no. 1322. Lunar and Planetary Institute, Woodlands, Texas.

Fischer, R.A., Campbell, A.J., and Ciesla, F.J. (2017) Sensitivities of Earth's core and mantle compositions to accretion and differentiation processes. Earth and Planetary Science Letters, 458, 252–262, https://doi.org/10.1016/j.epsl.2016.10.025.

Floss, C. (1999) Fe,Mg,Mn-bearing phosphates in the GRA 95209 meteorite: Occurrences and mineral chemistry. American Mineralogist, 84, 1354–1359, https://doi.org/10.2138/am-1999-0912.

Floss, C., Jolliff, B.L., Benedix, G.K., Stadermann, F.J., and Reid, J. (2007) Hammadah al Hamra 193: The first amphibole-bearing winonaite. American Mineralogist, 92, 460–467, https://doi.org/10.2138/am.2007.2253.

Fransolet, A.M., Fontan, F., Keller, P., and Antenucci, D. (1998) La Serie johnsomervilleite-fillowite dans les associations de phosphates de pegmatites granitiques de l'Afrique Centrale. Canadian Mineralogist, 36, 355–366.

Gattacceca, J., McCubbin, F.M., Grossman, J.N., Schrader, D.L., Chabot, N.L., D'Orazio, M., Goodrich, C., Greshake, A., Gross, J., Joy, K.H., and others. (2023) The Meteoritical Bulletin, No. 111. Meteoritics & Planetary Science, 58, 901–904, https://doi.org/10.1111/maps.13995.

Grew, E.S., Armbruster, T., Medenbach, O., Yates, M.G., and Carson, C.J. (2006) Stornesite-(Y), $(Y,Ca)_{\square 2}Na_6$ $(Ca,Na)_8(Mg,Fe)_{43}(PO_4)_{36}$, the first terrestrial Mg-dominant member of the fillowite group, from granulite-facies paragneiss in the Larsemann Hills, Prydz Bay, East Antarctica. American Mineralogist, 91.8–9, 1412–1424.

Grew, E.S., Yates, M.G., Beane, R.J., Floss, C., and Gerbi, C. (2010) Chopinite-sarcopside solid solution, $[(Mg,Fe)_3](PO_4)_2$, in GRA95209, a transitional acapulcoite: Implications for phosphate genesis in meteorites. American Mineralogist, 95, 260–272.

Hatert, F., Grew, E.S., Vignola, P., Rotiroti, N., Nestola, F., Keller, P., Baijot, M., Bruni, Y., Fransolet, A.M., Dal Bo, F., and others. (2021) Crystal chemistry and nomenclature of fillowite-type phosphates. Canadian Mineralogist, 59, 781–796, https://doi.org/10.3749/canmin.2000043.

Hunt, A.C., Benedix, G.K., Hammond, S.J., Bland, P.A., Rehkämper, M., Kreissig, K., and Strekopytov, S. (2017) A geochemical study of the winonaites: Evidence for limited partial melting and constraints on the precursor composition. Geochimica et Cosmochimica Acta, 199, 13–30, https://doi.org/10.1016/j.gca.2016.10.043.

Hunt, A.C., Cook, D.L., Lichtenberg, T., Reger, P.M., Ek, M., Golabek, G.J., and Schönbächler, M. (2018) Late metal-silicate separation on the IAB parent asteroid: Constraints from combined W and Pt isotopes and thermal modelling. Earth and Planetary Science Letters, 482, 490–500, https://doi.org/10.1016/j.epsl.2017.11.034.

Jones, R.H., McCubbin, F.M., Dreeland, L., Guan, Y., Burger, P.V., and Shearer, C.K. (2014) Phosphate minerals in LL chondrites: A record of the action of fluids during metamorphism on ordinary chondrite parent bodies. Geochimica et Cosmochimica Acta, 132, 120–140, https://doi.org/10.1016/j.gca.2014.01.027.

Jones, R.H., McCubbin, F.M., and Guan, Y. (2016) Phosphate minerals in the H group of ordinary chondrites, and fluid activity recorded by apatite heterogeneity in the Zag H3–6 regolith breccia. American Mineralogist, 101, 2452–2467.

Karwowski, Ł., Kusz, J., Muszyński, A., Kryza, R., Sitarz, M., and Galuskin, E.V. (2015) Moraskoite, $Na_2Mg(PO_4)F$, a new mineral from the Morasko IAB-MG iron meteorite (Poland). Mineralogical Magazine, 79, 387–398, https://doi.org/10.1180/minmag.2015.079.2.16.

Karwowski, Ł., Kryza, R., Muszyński, A., Kusz, J., Helios, K., Drożdżewski, P., and Galuskin, E.V. (2016) Czochralskiite, $Na_4Ca_3Mg(PO_4)_4$, a second new mineral from the Morasko IAB-MG iron meteorite (Poland). European Journal of Mineralogy, 28, 969–977, https://doi.org/10.1127/ejm/2016/0028-2557.

Lanari, P., Vidal, O., De Andrade, V., Dubacq, B., Lewin, E., Grosch, E.G., and Schwartz, S. (2014) XMapTools: A MATLAB©-based program for electron microprobe X-ray image processing and geothermobarometry. Computers & Geosciences, 62, 227–240, https://doi.org/10.1016/j.cageo.2013.08.010.

Lanari, P., Vho, A., Bovay, T., Airaghi, L., and Centrella, S. (2019) Quantitative compositional mapping of mineral phases by electron probe micro-analyser. Geological Society Special Publication, 478, 39–63.

Li, S., Wang, S., Bao, H., Miao, B., Liu, S., Coulson, I.M., Li, X., and Li, Y. (2011) The Antarctic achondrite, Grove Mountains 021663: An olivine-rich winonaite. Meteoritics & Planetary Science, 46, 1329–1344, https://doi.org/10.1111/j.1945-5100.2011.01232.x.

Litasov, K.D. and Podgornykh, N.M. (2017) Raman spectroscopy of various phosphate minerals and occurrence of tuite in the Elga IIE iron meteorite. Journal of Raman Spectroscopy, 48, 1518–1527, https://doi.org/10.1002/jrs.5119.

Lucas, M.P., Dygert, N., Ren, J., Hesse, M.A., Miller, N.R., and McSween, H.Y. (2020) Evidence for early fragmentation-reassembly of ordinary chondrite (H, L, and LL) parent bodies from REE-in-two-pyroxene thermometry. Geochimica et Cosmochimica Acta, 290, 366–390, https://doi.org/10.1016/j.gca.2020.09.010.

McCoy, T.J. and Carlson, W.D. (1998) Opaque minerals in the GRA 95209 lodranite: A snapshot of metal segregation. Proceedings of the 29th Lunar and Planetary Science Conference, p. 1675. Lunar and Planetary Institute, Woodlands, Texas.

McCoy, T.J., Steele, I.M., Keil, K., Leonard, B.F., and Endress, M. (1994) Chladniite, $Na_2CaMg_7(PO_4)_6$: A new mineral from the Carlton (IIICD) iron meteorite. American Mineralogist, 79, 375–380.

McCoy, T.J., Carlson, W.D., Nittler, L.R., Stroud, R.M., Bogard, D.D., and Garrison, D.H. (2006) Graves Nunataks 95209: A snapshot of metal segregation and core formation. Geochimica et Cosmochimica Acta, 70, 516–531, https://doi.org/10.1016/j.gca.2005.09.019.

McCubbin, F.M. and Jones, R.H. (2015) Extraterrestrial apatite: Planetary geochemistry to astrobiology. Elements, 11, 183–188, https://doi.org/10.2113/gselements.11.3.183.

McCubbin, F.M. and Ustunisik, G. (2018) Experimental investigation of F and Cl partitioning between apatite and Fe-rich basaltic melt at 0 GPa and 950–1050 °C: Evidence for steric controls on apatite-melt exchange equilibria in OH-poor apatite. American Mineralogist, 103, 1455–1467, https://doi.org/10.2138/am-2018-6339.

McCubbin, F.M., Riner, M.A., Vander Kaaden, K.E., and Burkemper, L.K. (2012) Is Mercury a volatile-rich planet? Geophysical Research Letters, 39, 1–5, https://doi.org/10.1029/2012GL051711.

McCubbin, F.M., Lewis, J.A., Barnes, J.J., Elardo, S.M., and Boyce, J.W. (2021) The abundances of F, Cl, and $H_2O$ in eucrites: Implications for the origin of volatile depletion in the asteroid 4 Vesta. Geochimica et Cosmochimica Acta, 314, 270–293, https://doi.org/10.1016/j.gca.2021.08.021.

McCubbin, F.M., Lewis, J.A., Barnes, J.J., Boyce, J.W., Gross, J., Mccanta, M.C., Srinivasan, P., Anzures, B.A., Lunning, N.G., Elardo, S.M., and others. (2023) On the origin of fluorine-poor apatite in chondrite parent bodies. American Mineralogist, 108, 1185–1200, https://doi.org/10.2138/am-2022-8623.

Nittler, L.R., Boujibar, A., Crapster-Pregont, E., Frank, E.A., McCoy, T.J., McCubbin, F.M., Starr, R.D., Vorburger, A., and Weider, S.Z. (2023) Chromium on Mercury: New results from the MESSENGER X-ray spectrometer and implications for the innermost planet's geochemical evolution. Journal of Geophysical Research: Planets, 128, e2022JE007691.

Pan, Y. and Fleet, M.E. (2002) Compositions of the apatite-group minerals: Substitution mechanisms and controlling factors. In M.J. Kohn, J. Rakovan, and J.M. Hughes, Eds., Phosphates, p. 13–50, https://doi.org/10.1515/9781501509636-005.

Pasek, M.A. (2015) Phosphorus as a lunar volatile. Icarus, 255, 18–23, https://doi.org/10.1016/j.icarus.2014.07.031.

Patiño Douce, A.E. and Roden, M. (2006) Apatite as a probe of halogen and water fugacities in the terrestrial planets. Geochimica et Cosmochimica Acta, 70, 3173–3196, https://doi.org/10.1016/j.gca.2006.03.016.

Piccoli, P.M. and Candela, P.A. (2002) Apatite in igneous systems. Reviews in Mineralogy and Geochemistry, 48, 255–292, https://doi.org/10.2138/rmg.2002.48.6.

Prior, D.J., Boyle, A.P., Brenker, F., Cheadle, M.C., Austin, D., Lopez, G., Peruzzo, L., Potts, G.J., Reddy, S., Spiess, R., and others. (1999) The application of electron backscatter diffraction and orientation contrast imaging in the SEM to textural problems in rocks. American Mineralogist, 84, 1741–1759.

Righter, K., Sutton, S.R., Danielson, L., Pando, K., and Newville, M. (2016) Redox variations in the inner solar system with new constraints from vanadium XANES in spinels. American Mineralogist, 101, 1928–1942, https://doi.org/10.2138/am-2016-5638.

Sarafian, A.R., John, T., Roszjar, J., and Whitehouse, M.J. (2017) Chlorine and hydrogen degassing in Vesta's magma ocean. Earth and Planetary Science Letters, 459, 311–319, https://doi.org/10.1016/j.epsl.2016.10.029.

Tartèse, R., Anand, M., and Franchi, I.A. (2019) H and Cl isotope characteristics of indigenous and late hydrothermal fluids on the differentiated asteroidal parent body of Grave Nunataks 06128. Geochimica et Cosmochimica Acta, 266, 529–543, https://doi.org/10.1016/j.gca.2019.01.024.

Vallcorba, O., Casas, L., Colombo, F., Frontera, C., and Rius, J. (2017) First terrestrial occurrence of the complex phosphate chladniite: Crystal-structure refinement by synchrotron through-the-substrate microdiffraction. European Journal of Mineralogy, 29, 287–293, https://doi.org/10.1127/ejm/2017/0029-2590.

Voshage, H. (1967) Bestrahlungsalter und Herkunft der Eisenmeteorite. Zeitschrift für Naturforschung—Section A Journal of Physical Sciences, 22, 477–506, https://doi.org/10.1515/zna-1967-0410.

Ward, D., Bischoff, A., Roszjar, J., Berndt, J., and Whitehouse, M.J. (2017) Trace element inventory of meteoritic Ca-phosphates. American Mineralogist, 102, 1856–1880, https://doi.org/10.2138/am-2017-6056.

Webster, J.D. and Piccoli, P.M. (2015) Magmatic apatite: A powerful, yet deceptive, mineral. Elements, 11, 177–182, https://doi.org/10.2113/gselements.11.3.177.

Xie, X., Yang, H., Gu, X., and Downs, R.T. (2015) Chemical composition and crystal structure of merrillite from the Suizhou meteorite. American Mineralogist, 100, 2753–2756.

Zeng, X., Shang, Y., Li, S., Li, X., Wang, S., and Li, Y. (2019) The layered structure model for winonaite parent asteroid implicated by textural and mineralogical diversity. Earth, Planets, and Space, 71, 38, https://doi.org/10.1186/s40623-019-1015-9.

Zolotov, M.Y., Sprague, A.L., Hauck, S.A. II, Nittler, L.R., Solomon, S.C., and Weider, S.Z. (2013) The redox state, FeO content, and origin of sulfur-rich magmas on Mercury. Journal of Geophysical Research. Planets, 118, 138–146, https://doi.org/10.1029/2012JE004274.

Manuscript received September 18, 2023
Manuscript accepted January 25, 2024
Accepted manuscript online February 7, 2024
Manuscript handled by Oliver Tschauner

## Endnote:

[1]Deposit item AM-24-99195. Online Materials are free to all readers. Go online, via the table of contents or article view, and find the tab or link for supplemental materials.